Journal of Industrial and Engineering Chemistry 51 (2017) 153–161

Contents lists available at ScienceDirect

Journal of Industrial and Engineering Chemistry

journal homepage: www.elsevier.com/locate/jiec

Study on the effect of current collector structures on the performance of MCFCs using three-dimensional fluid dynamics analysis

Chang-Whan Lee[a], Mihui Lee[b], Sung-Pil Yoon[b], Hyung-Chul Ham[b], Sun Hee Choi[b,*], Jonghee Han[b,*], Suk Woo Nam[b], Dong-Yol Yang[c]

[a] Department of Mechanical System and Design Engineering, Seoul National University of Science and Technology, Gongneung-ro 232, Nowon-gu, Seoul, 139-743, South Korea
[b] Fuel Cell Research Center, KIST, Hwarangno 14-gil 5, Seongbuk-gu, Seoul 136-791, South Korea
[c] School of Mechanical Engineering & Aerospace System, KAIST, Daehak-ro 291, Yuseong-gu, Daejeon 305-701, South Korea

ARTICLE INFO

Article history:
Received 4 January 2017
Received in revised form 16 February 2017
Accepted 25 February 2017
Available online 6 March 2017

Keywords:
MCFC
Polarization
Current collector
CFD

ABSTRACT

The effect of current collectors of molten carbonate fuel cells (MCFCs) was studied through three-dimensional computational fluid dynamics and experiments. Three types of current collectors such as a sheet with sheared protrusions and perforated sheets were employed and performances of MCFCs were compared. A current collector structure with a large gas open area to electrodes improves diffusion characteristics between electrodes and gas flow channels. As a result, differences of gas mole fractions between gas flow channels and electrodes were decreased. Finally, Nernst loss and cathode polarization loss decreased, and the performance was enhanced. Using these results, current collector structures for improved performance and long-term operation were discussed.
© 2017 The Korean Society of Industrial and Engineering Chemistry. Published by Elsevier B.V. All rights reserved.

Introduction

Molten carbonate fuel cells (MCFCs) were developed to produce clean and efficient power conversion. MCFCs are fuel cells with high-temperature and employ molten carbonate electrolytes [1]. A ceramic ($LiAlO_2$) matrix contains liquid electrolytes between the electrodes. Fig. 1 presents the schematic figure of MCFCs.

The anode gas and cathode gas flow through gas flow channels and current collectors. Gas flow channels and current collectors influence fuel gas supplies to reaction sites [2]. As a result, the gas flow characteristics are important on the performance [3,4]. There are numerous studies to investigate effects of flow characteristics on solid oxide fuel cells (SOFCs) [2], direct methanol fuel cells (DMFCs) [4–6], and polymer membrane fuel cells (PEMFCs) [7–10].

In MCFCs, numerical studies were performed to study effects of flow characteristics on the performance of MCFCs. Hirata et al. [11] evaluated relationship between the gas channel and diffusion characteristics. Flow characteristics were evaluated using computational fluid dynamics (CFD) analysis and diffusion was evaluated using an analytic model. Yoshiba et al. [12] investigated performances of MCFC stack for various gas-flow types by a numerical model. Ma et al. [13] investigated effects of non-uniform inlet flow rates on the fuel cell numerically. Kim et al. [14] calculated the MCFC stack performance by assuming the current collector as a porous media, which shows the equivalent gas flow property. The gas flow in the porous media, were modeled with Darcy's law [15]. The equivalent properties of a porous media such as the inertial resistance and the effective permeability are calculated from the CFD analysis.

In this work, effects of the current collector structures on MCFCs were studied. In the simulation model, the current collector and the flow channel were three-dimensionally modeled. Three types of current collectors were employed in the experiments and simulation. For precise prediction of the temperature distribution, detailed flow characteristics and the interaction between electrodes and current collectors [16,17] were considered. For the verification of the simulation model and further investigation on the effect of the current collector, experiments were conducted. Distributions of gas concentrations, current densities, and polarization components were investigated using the simulation

* Corresponding authors. Fax: +82 2 958 5199.
E-mail addresses: shchoi@kist.re.kr (S.H. Choi), jhan@kist.re.kr (J. Han).

http://dx.doi.org/10.1016/j.jiec.2017.02.026
1226-086X/© 2017 The Korean Society of Industrial and Engineering Chemistry. Published by Elsevier B.V. All rights reserved.

Nomenclature

c_j	Molar concentration of species j
C_p	Specific heat capacity ($J\,kg^{-1}\,K^{-1}$)
D_j	Diffusion coefficient of species *j* ($m^2\,s^{-1}$)
E_0	Standard potential (V)
E_{eq}	Equilibrium cell potential (V)
F	Faraday's constant ($96485\,C\,mol^{-1}$)
h	Heat transfer coefficient ($W\,m^{-2}\,K^{-1}$)
i	Local current density ($mA\,cm^{-2}$)
i_{avg}	Average current density ($mA\,cm^{-2}$)
k_j	Thermal conductivity of species *j* ($W\,m^{-1}\,K^{-1}$)
m_j	Mass fraction of species *j*
M_j	Molecular weight of species *j* ($g\,mol^{-1}$)
p_j	Partial pressure of species j ($N\,m^{-2}$)
P	Total pressure ($N\,m^{-2}$)
R	Universal gas constant ($8.3145\,J\,mol^{-1}\,K^{-1}$)
R_a	Anode polarization resistance ($\Omega\,m^2$)
R_c	Cathode polarization resistance ($\Omega\,m^2$)
R_{irr}	Total polarization resistance ($\Omega\,m^2$)
R_{ohm}	Ohmic resistance ($\Omega\,m^2$)
S_j	Source term of j_{th} equation
T	Temperature (K)
u_j	Velocity of species *j* ($m\,s^{-1}$)
V_{cell}	Cell voltage (V)
X_j	Mole fraction of species *j*

Greek symbols

μ_i	Dynamic viscosity of species i ($kg\,m^{-1}\,s^{-1}$)
ν_i	Kinematic viscosity of species i ($kg\,m^{-1}\,s^{-1}$)
ρ	Density of the gas ($kg\,m^{-3}$)

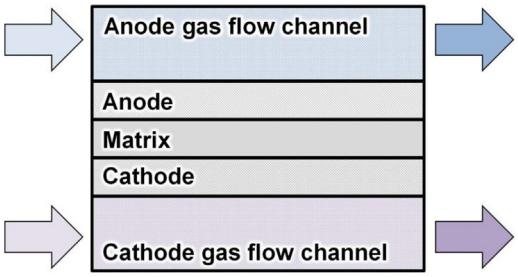

Fig. 1. Schematic figure of MCFCs.

results. Finally, current collector structures for better long-term operations and high performance were discussed.

Experimental set-up

Operation of the 100 cm^2 single cell for MCFCs

In the operation of the single cell for MCFCs, a Ni—5 wt% Al anode, a lithiated NiO cathode, and γ-$LiAlO_2$ matrices were used. For the electrolyte, Li_2CO_3 and K_2CO_3 (62:38) were used [18]. The operation temperature of the single cell was 620° C. Gas utilizations for the anode and cathode sides were fixed to 0.4 at 150 mA/cm^2. Operating conditions are listed in Table 1. Cell frames with internal flow channels were utilized in experiments, because cell frames with internal flow channels had advantages in controlling temperatures of the cell frame and components [18]. The size of the cell frame was 130 mm (length) × 130 mm (width) × 30 mm (height). The active area of the single cell was 100 cm^2.

Table 1
Operating condition of MCFCs.

Temperature		620 °C
Pressure		1 atm
Sealing pressure		0.2 MPa
Gas utilization (Anode H_2/cathode O_2 and CO_2)		0.4 at 150 mA/cm^2
Gas flow rate		Anode Cathode
Gas composition	Anode	H_2:CO_2:H_2O = 0.72:0.18:0.1
	Cathode	Air:CO_2 = 0.7:0.3

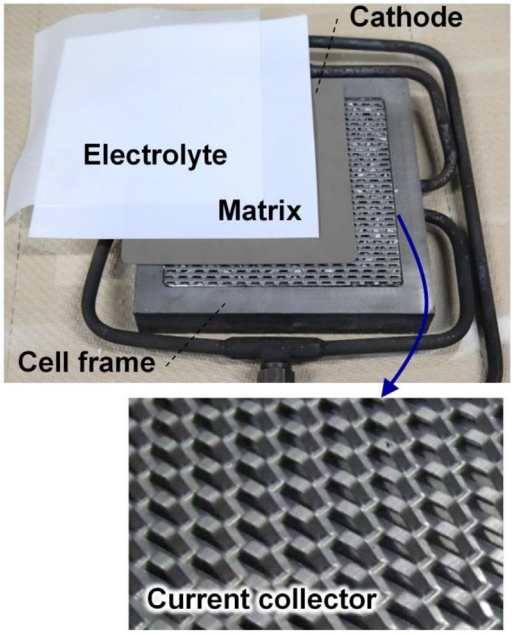

Fig. 2. Cell frame and the components of MCFCs.

The cell frame and components such as electrolytes, a matrix, a cathode and a cathode current collector are shown in Fig. 2. In order to secure close contacts among components, a sealing pressure with a value of 0.2 MPa was applied to the cell frame.

Current collector structures

In MCFCs, there are two major types of current collectors [19]. The first type of current collectors employs a sheet with sheared protrusions as a current collector and a gas flow channel. In the first type of current collector, gas flow channels were formed by the sheet with sheared protrusions. The second type of current collectors employs a perforated sheet as a current collector. In this type of the current collector, the gas flow channel was formed in the cell frame instead of using the sheet with sheared protrusions. The perforated sheet is placed on the gas flow channel for the stable operation of the electrode [18].

In this work, three kinds of current collectors were employed to investigate effects of current collectors on MCFCs. Current collectors of three cases are shown in Fig. 3(a)–(c). In CC1 and CC2, the sheet with sheared protrusions [20] (also called as a shielded slot plate) were employed to the current collector. Gas flow channels were formed by the sheet with sheared protrusion. The flow channel in the cell frame is not required. In CC3, the flow

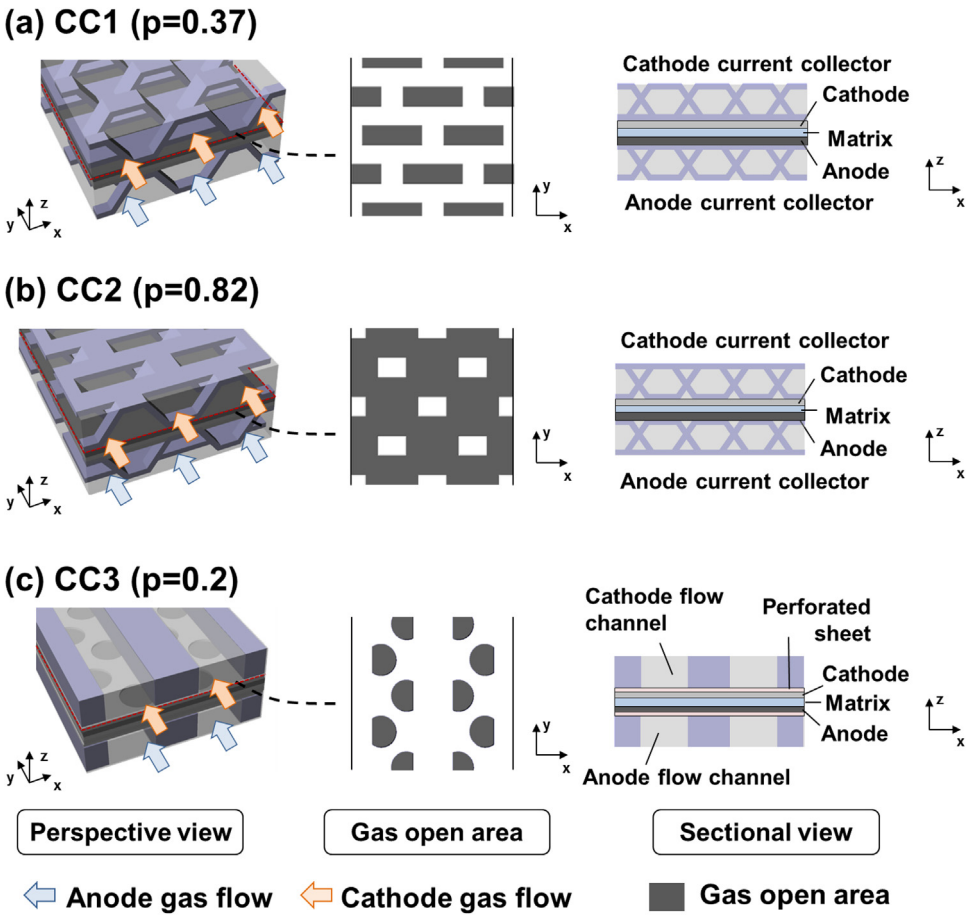

Fig. 3. Current collectors of three cases: (a) CC1, (b) CC2, and (c) CC3.

channels were formed in the cell frame and the perforated sheet was employed in the current collector.

The difference between CC1 and CC2 was the stacking direction of the current collector. In CC1, the base region of the sheet, where the sheared protrusions were not formed, made contact with electrodes. The upper flat surface of the sheared protrusions made contact with the cell frame. On the contrary, in CC2, the upper flat surface of the sheared protrusions made contact with electrodes. The gas open area of the cathode and anode is different. The perforated ratio (p) was the ratio of the area of gas open area to the total area of electrodes. The perforated ratios are 0.37 in CC1 and 0.82 in CC2.

In CC3, the perforated sheet and the cell frame with flow channels were used for the comparison. The gas flow channel was formed in the cell frame [18]. The perforated sheet was employed in the current collector. In this case, the perforated ratio is 0.2.

Simulation model for MCFCs

Calculation of the current density

Reactions of MCFCs are presented in Eq. (1). The carbonate ion (CO_3^{2-}) acts as an electric charge carrier. In the anode side, H_2 reacts with CO_3^{2-} to produce H_2O and CO_2.

$$\begin{aligned} &\text{Anode side}: CO_3^{2-} + H_2 \rightarrow CO_2 + H_2O + 2e^- \\ &\text{Cathode side}: \frac{1}{2}O_2 + CO_2 + 2e^- \rightarrow CO_3^{2-} \end{aligned} \quad (1)$$

In the anode side, water–gas shift (WGS) reaction takes place. WGS reaction reaches equilibrium very quickly. The equilibrium constant of WGS reaction is presented in Eq. (3).

$$\text{Anode side}: H_2O + CO \leftrightarrow CO_2 + H_2 \quad (2)$$

$$\begin{aligned} K_{WGS} &= \frac{[P_{H_2}][P_{CO_2}]}{[P_{CO}][P_{H_2O}]} \\ &= 157.02 - 0.4447T + 4.2777 \times 10^{-4}T^2 - 1.3871 \times 10^{-7}T^3 \end{aligned} \quad (3)$$

In this work, electrochemical reaction is assumed to occur on the matrix surface which is called as the reaction surface. All variables related with electrochemical reactions were calculated on the reaction surface. The standard potential (E_0) of MCFCs is calculated from the difference of molar Gibbs free energy (ΔG) as shown in Eq. (4).

$$\begin{aligned} E_0^{x,y} &= -\frac{\Delta G}{2F} \\ &= -\frac{-243730 + 48.996 \times T^{x,y} + 2.474 \times 10^{-3} \times (T^{x,y})^2}{2F} \end{aligned} \quad (4)$$

The equilibrium cell potential (E_{eq}) of MCFCs is calculated from the partial pressures of anode gases and cathode gases and the standard potential (E_0). E_{eq} is expressed as follows:

$$E_{eq}^{x,y} = E_0^{x,y} + \frac{RT}{2F}\ln\left(\frac{P_{H_2,a}^{x,y} P_{CO_2,c}^{x,y} \sqrt{P_{O_2,c}^{x,y}}}{P_{H_2O,a}^{x,y} P_{CO_2,a}^{x,y}}\right) \quad (5)$$

The open circuit voltage of the cell (E_{OCV}) was calculated from Eq. (5). In the simulation, the voltage of the cell was assumed to be uniform with the value of V_{cell} at the reaction surface [21]. The polarization model by Yuh and Selman [22] was adopted In the numerical models for polarization of MCFCs. In this polarization model, polarization components were composed of anode polarization resistance (R_a), cathode polarization resistance (R_c) and ohmic resistance (R_{ohm}) [22]. Each polarization terms were derived experimental results with various operating conditions. The ohmic loss in Eq. (7) was modeled with an Arrhenius type equation and previous experimental results [23]. The local current density ($i^{x,y}$) was calculated using Eq. (4).

$$R_a^{x,y} = 2.27 \times 10^{-9}\exp\left(\frac{6435}{T^{x,y}}\right)\left(P_{H_2}^{x,y}\right)^{-0.42}\left(P_{CO_2}^{x,y}\right)^{-0.17}\left(P_{H_2O}^{x,y}\right)^{-1.0}[\Omega m^2] \quad (6)$$

$$R_c^{x,y} = 7.505 \times 10^{-10}\exp\left(\frac{9298}{T^{x,y}}\right)\left(P_{O_2}^{x,y}\right)^{-0.43}\left(P_{CO_2}^{x,y}\right)^{-0.09}[\Omega m^2] \quad (7)$$

$$R_{ohm}^{x,y} = 0.32 \times 10^{-4}\exp\left[4026\left(\frac{1}{T^{x,y}} - \frac{1}{923}\right)\right][\Omega m^2] \quad (8)$$

$$i^{x,y} = \frac{E_{eq}^{x,y} - V_{cell}}{R_{irr}^{x,y}} = \frac{E_{eq}^{x,y} - V_{cell}}{R_a^{x,y} + R_c^{x,y} + R_{ohm}^{x,y}} \quad (9)$$

In the previous study [18], polarization models in Eqs. (6)–(8) were verified with respect to operating temperatures (650 °C, 620 °C, 600 °C, and 580 °C), gas utilizations (0.4, 0.6, and 0.8), and various gas compositions. The simulation model predicted the performance of 100 cm^2 MCFC cells precisely when the concentration loss is not dominant.

Governing equations for momentum conservation, continuity, species and energy are presented in Eqs. (10)–(13) [14].

$$\frac{\partial}{\partial x_j}(\rho u_j u_i) = -\frac{\partial P}{\partial x_i} + \frac{\partial}{\partial x_j}(\mu\frac{\partial u_i}{\partial x_j}) + S_i \quad (10)$$

$$\frac{\partial}{\partial x_j}(\rho u_j) = \pm m_{co_3^{2-}} \quad (11)$$

$$\frac{\partial}{\partial x_j}(\rho u_j m_k) = \frac{\partial}{\partial x_j}(\rho D_{j,k}\frac{\partial m_k}{\partial x_j}) + S_k \quad (12)$$

$$u_j\frac{\partial(\rho C_P T_g)}{\partial x_j} = \frac{\partial}{\partial x_j}(k_j\frac{\partial T_g}{\partial x_j}) - \sum_k h_k(T_g - T_k) + \sum Q \quad (13)$$

where u_j is a velocity of the species j, m_k is a mass fraction of species k, S_j is a net mass production of species j, $D_{j,k}$ is a multi-component diffusivity, and Q is the heat generation per unit volume.

Electrochemical reactions occur on the reaction surface. The reaction surface acts as mass sources of species. The source term on the reaction surface is proportional to $i^{x,y}$ and expressed as follows:

$$\text{Anodeside}: \quad D_{H_2}\frac{\partial c_{H_2}}{\partial z} = \frac{i}{2F}$$
$$\text{Cathodeside}: \quad D_{O_2}\frac{\partial c_{O_2}}{\partial z} = \frac{i}{4F} \quad (14)$$

The composition and properties of mixture gases varies with respect to the temperature, gas compositions, and electrochemical reactions. In the calculation of the mixture gas properties such as compositions of mixture gases, the specific heat (C_p), thermal conductivity (k), density (ρ), viscosity (μ) and was considered [24]. The density (ρ) and specific heat (C_p), of mixture gas were calculated from the ideal gas law. Using the gas mixture rule, the viscosity (μ) and thermal conductivity (k) of the mixture gas were calculated.

Simulation model

In the simulation, it was not possible to consider the full model of a 100 cm^2 single cell (100 mm × 100 mm) with current collector. To simplify the simulation model, a simplified model using periodic boundary conditions was employed [25,26], because the gas flow channels formed by the current collector are repeated structures. In the simulation, the length of the gas flow direction was 48 mm and nearly half of that of the single cell. In the transverse direction to the gas flow channel, two unit structures of the sheared protrusions were employed. The active area of the simulation model was 576 mm^2. In the planes, x = 0 mm and 12 mm were selected as planes on the periodic boundary condition.

For the precise simulation, the gas flow channel was meshed using very fine tetrahedral elements. The simulation model of CC2 is presented in Fig. 4. The gas flow channel formed by the current collector is also shown in Fig. 4. In the simulation model, 504,827 tetrahedral elements for CC1, 486,130 elements for CC2, 509,124 tetrahedral elements for CC3 were used.

Gas flows in gas flow channels were assumed to be laminar flow due to low Reynolds number [18]. Heat generation due to the electrochemical reaction was not considered, because temperature change of the cell is less than 1 °C in a 100 cm^2 single cell [18]. In the anode flow channel, a water-gas shift (WGS) reaction occurred. The WGS reaction reached equilibrium before the gases were inserted into the cell frame [27]. The composition of the anode input gas at 620 °C was H_2:CO_2:H_2O:CO = 0.617:0.077:0.203:0.103.

The commercial CFD code COMSOL multi-physics v14 [28] was employed in order to calculate the steady state conditions, such as mole fraction of gases, flow field and distribution of the current density. The calculation begins with given cell voltages (V_{cell}). When the relative error was less than relative tolerance (10^{-4}), the solution was converged. By averaging the local current density, the average current density (i_{avg}) was obtained. Finally, performance of the cell such as I–V curve was obtained.

Simulation and experimental results

I–V characteristics

The performances of the simulation model were compared with experimental results for verification. Experiments were repeated 5 times and the voltage difference in experiments at 150 mA/cm^2 was less than 3 mV, which is less than 0.5% of the cell voltage at 150 mA/cm^2. I–V curves in Fig. 5 were the average value of experiments. Fig. 5 shows I–V characteristics of CC1, CC2 and CC3. In experiments, the values of voltage at 150 mA/cm^2 for CC1, CC2 and CC3 were 0.821 V, 0.834 V and 0.813 V, respectively. In simulation results, the values of voltage at 150 mA/cm^2 for CC1, CC2, and CC3 were 0.823 V, 0.832 V, and 0.816 V, respectively. The maximum difference between the calculated and experimental results was 3 mV. Simulation results are in close agreements with experimental results.

As shown in Fig. 5, voltages of CC1 and CC2 were higher than the voltage of CC3. A cell with the sheet with sheared protrusions

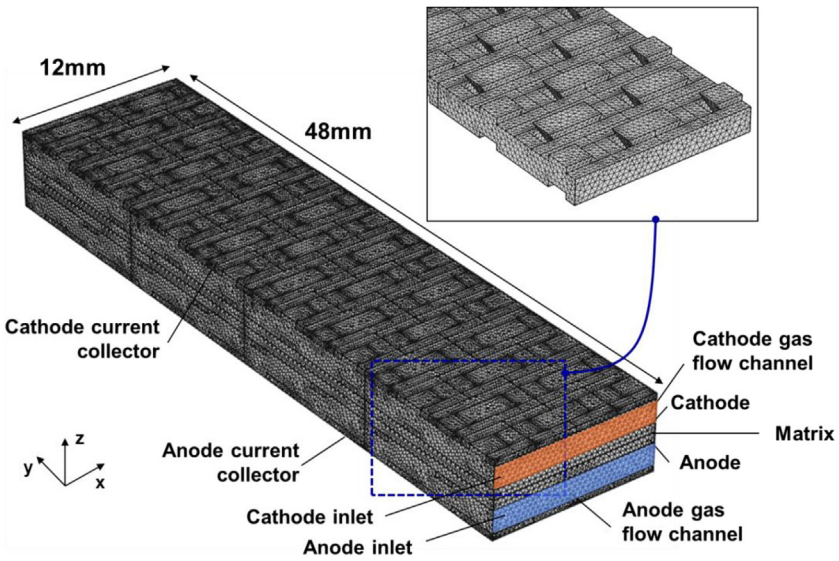

Fig. 4. Mesh of CC2 and gas flow channels of the cathode side formed by the cathode current collector.

shows better performance. The voltage of CC2 was higher than that of CC1. The difference between CC1 and CC2 was the open surface area. The current collector that has a large open area to the electrode shows better performance.

Polarization components with different geometries of current collectors

The polarization components of the single cell cases were studied numerically. The polarization components in the simulation were composed of the ohmic loss, Nernst loss, the anode polarization loss, and the cathode polarization loss. Nernst loss was calculated as differences of equilibrium potentials between the gas inlet and the gas outlet [29].

Table 2 shows Voltage of the cell at 150 mA/cm^2 and calculated polarization components. In the polarization components, Nernst loss and the cathode polarization loss showed a large difference among the three cases. The differences of Nernst loss and the cathode polarization loss between CC2 and CC3 were 10.72 mV and 6.03 mV, respectively. Differences in the anode polarization loss among the three cases were less than 1 mV. The current collector had little effect on the ohmic loss and the anode polarization loss of MCFCs.

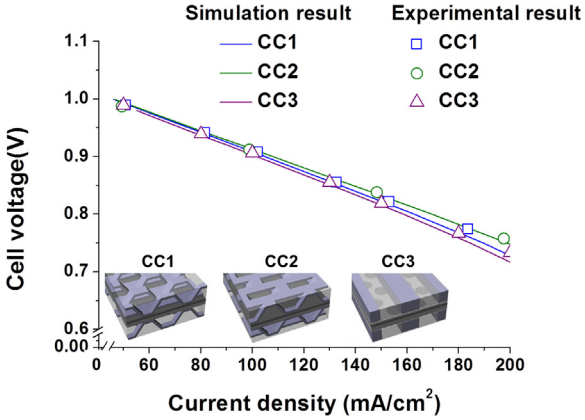

Fig. 5. I–V characteristics of CC1, CC2, and CC3: comparison of simulation results with experimental results.

From these results, difference of performances in CC1, CC2, and CC3 was induced from Nernst loss and the cathode polarization loss. When the gas open area is large (CC2), fuel gases can be supplied to the electrode and the reaction area efficiently. As a result, the current collector with large gas open areas minimizes the cathode polarization loss.

The ohmic resistance (internal resistance) was measured using Solatron S1287 and 1255B by an electrochemical impedance spectroscopy analysis. The value of internal resistances of CC1, CC2 and CC3 was 3.9 mΩ, 4.1 mΩ, and 3.8 mΩ, respectively. Like the ohmic resistances in the simulation results, in the internal resistance in CC1, case and CC3, there were no significant differences.

By the gas analyzer (Agilent 7890B GC), the N_2 crossover was measured at the anode gas outlet. From the N_2 crossover, the gas crossover from the cathode side to the anode side was measured [30]. The measured N_2 cross-over at the anode gas exit of CC1, CC2, and CC3 was 0.34%, 0.32% and 0.36%, respectively. In the three cases, there were no significant differences in the N_2 cross-over at the anode gas exit. From these results, three single cells of CC1, CC2, and CC3 were operated without any problems.

Gas distributions and related characteristics

From the simulation, the performance, flow field, and gas mole fractions of three cases were investigated. Velocity distributions of CC2 at 150 mA/cm^2 were compared. Fig. 6 shows the distribution of the velocity magnitude. Figures were drawn at the center of the gas flow channel. As shown in Fig. 6(a), in anode flow channels, the velocity magnitude increased, because H_2O and CO_2 were generated from H_2 and CO_3^{2-}. Conversely, in cathode flow channels, velocity magnitude decreased, because CO_2 and O_2 were consumed in the reaction of MCFCs.

Fig. 7 presents H_2 mole fractions at 150 mA/cm^2 in anode flow channels for three cases. Fig. 8 presents O_2 mole fractions at 150 mA/cm^2 in cathode flow channels for three cases. Along the gas flow direction, H_2 mole fractions decreased due to the electrochemical reaction. The contour of the H_2 mole fraction showed wavy shapes in CC1 and CC3. Wavy shapes of the cathode flow were heavier than that of the anode flow, because diffusion coefficient of the anode gas ($D_{H2} = 4.615 \times 10^{-4}$ m^2/s) is smaller than cathode gas ($D_{CO2} = 1.183 \times 10^{-4}$ m^2/s). The wavy shape of the gas mole fraction means that the gas was not sufficiently supplied

Table 2
Voltage of the cell at 150 mA/cm^2 and calculated polarization components.

	Voltage at 150 mA/cm^2 (V)	Polarization components at 150 mA/cm^2			
		Cathode polarization loss (mV)	Nernst loss (mV)	Ohmic loss (mV)	Anode polarization loss (mV)
CC1	0.823	105.62	70.70	55.67	29.90
CC2	0.832	102.10	65.66	55.67	29.78
CC3	0.816	108.13	76.38	55.67	29.15

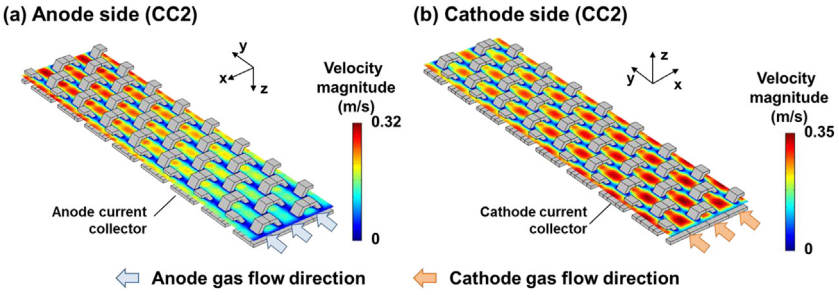

Fig. 6. Velocity distribution of CC2 at 150 mA/cm^2: (a) Anode side and (b) Cathode side.

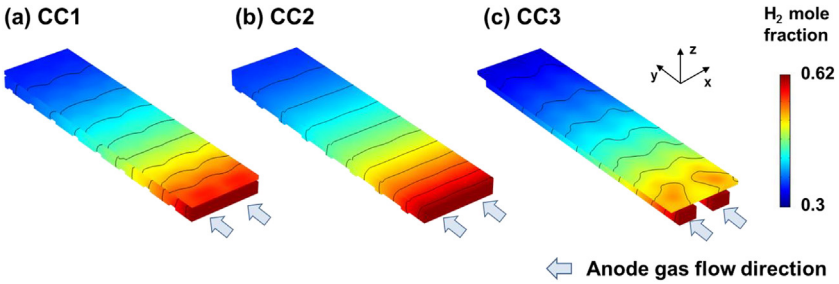

Fig. 7. H_2 mole fraction at 150 mA/cm^2 in anode flow channels.

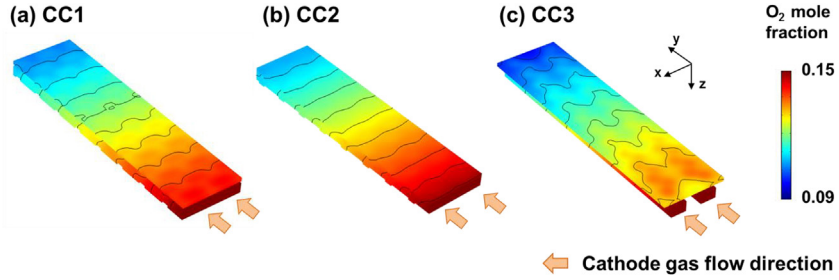

Fig. 8. O_2 mole fraction at 150 mA/cm^2 in cathode flow channels.

in the transverse direction. In CC2, the contour of H_2 mole fraction was nearly perpendicular to the gas flow direction. These results indicate that a large gas open area (CC2) results in effective supply of fuel gas. Finally, the cathode polarization loss and Nernst loss were decreased.

Fig. 9 presents the distribution of E_{eq} (equilibrium cell potential) for CC1, CC2 and CC3 at the average current density of 150 mA/cm^2. Nernst loss had the largest effect on the performance with different types of current collectors. Distribution of E_{eq} was determined from gas mole fractions. At the gas inlet and outlet, CC2 showed the highest E_{eq} among three cases. Likewise distribution of the H_2 mole fraction in anode flow channels, the contour of E_{eq} in CC2 was nearly perpendicular to gas flow directions. When gas open areas of the current collector were large, the fuel gas was supplied effectively, and E_{eq} increased. Finally, Nernst loss decreased and performance of the cell increased.

Cathode side polarizations of CC1, CC2 and CC3 at 150 mA/cm^2 are shown in Fig. 10. The total polarizations of three cases at 150 mA/cm^2 are presented in Fig. 11. While anode polarization components had little effect on the performance, cathode polarization components had a significant effect on the performance. Total polarizations were nearly the same distribution with the cathode polarizations. The cathode polarization of CC2 showed the smallest value. The current collector which has a large gas open area to electrodes results in efficient gas supply and reduces the cathode polarization.

The distributions of the current density of three cases are shown in Fig. 12. When gas flow directions of the anode and

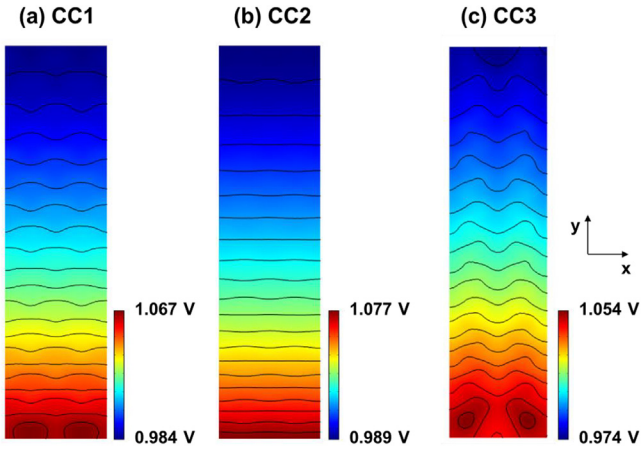

Fig. 9. Distribution of E_{eq} at 150 mA/cm^2.

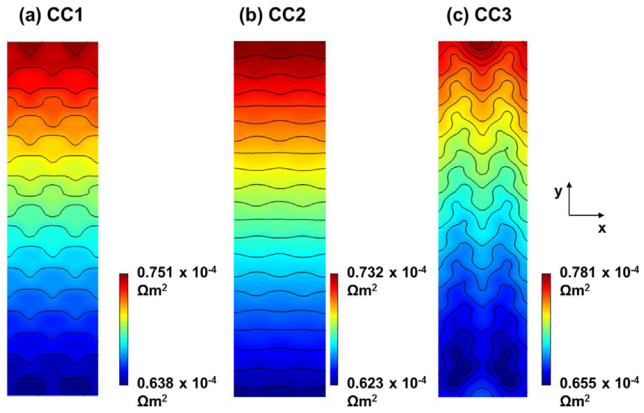

Fig. 10. Cathode polarization resistance at 150 mA/cm^2.

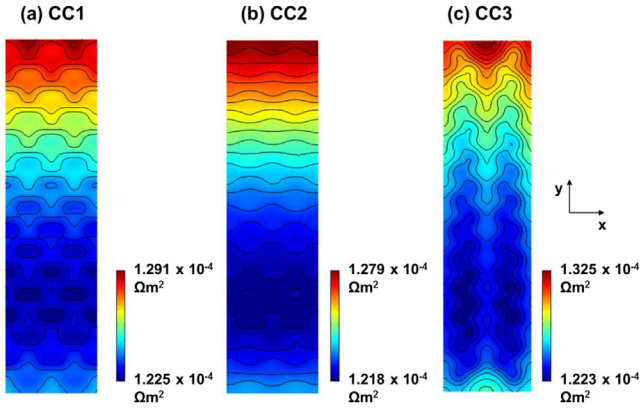

Fig. 11. Total polarization resistance at 150 mA/cm^2.

cathode gases were parallel, the current density decreased along gas flow directions. Like H_2 mole fraction distribution, a contour of the current density of CC2 was nearly perpendicular to the flow direction. Wavy shapes of contours of CC3 were heavier than that of CC1 and CC2 due to the heavier wavy shape of E_{eq} and the polarization of CC3. The current density of CC2 was more uniformly distributed than the current density of the other cases. Fuel gases were supplied efficiently by employing a current collector with a large gas open area.

Simulation results are summarized as follows: The current collector structure, which has a large gas open area to electrodes, leads to efficient gas supply to electrodes and reaction sites. Consequently, equilibrium cell potential (E_{eq}) increases. Nernst loss and the cathode polarization decreases. Among polarization components, Nernst loss had the largest effect on the performance. Finally, the performance of MCFCs becomes higher, and a more uniform electrochemical reaction occurs.

Discussion

Performance of MCFCs with respect to the perforated ratio of the perforated sheet

A simulation with respect to the perforated ratio (p) of the perforated sheet was conducted to investigate the effect of perforated ratio of the perforated sheet on the performance of MCFCs. The simulation condition was the same as CC3 except for the perforated sheet. The radius of the perforated circle in the current collector was determined based on the corresponding perforated ratio. With a higher perforated ratio, the radius of the perforated circle was larger.

Distribution of cell voltages at 150 mA/cm^2 according to the perforated ratios is presented in Fig. 13. The performance of the cell increased as the perforated ratio increased (i. e., the open surface of the electrode increased). When the perforated ratio was 0.5, the voltage of the cell at 150 mA/cm^2 was 0.818 V. When the perforated ratio was 0.7, the voltage of the cell at 150 mA/cm^2 was 0.819 V. The area of the open layer of the electrode for gas increased with increased value of the perforated ratio. With a larger value of the perforated ratio, more gases could be supplied to the electrodes effectively, resulted in an improved performance of MCFCs.

Distribution of the gas mole fraction in the thickness direction

Mole fractions of CO_2 on the cathode side were investigated. On surfaces of electrodes, electrochemical reaction of MCFCs occurs. Surfaces of electrodes act as mass sources or sinks. Mole fractions of CO_2 and O_2 at the cathode side decrease along gas flow directions (y-direction). There was a mole fraction distribution in the thickness direction (z-direction).

Fig. 14 shows the cross-section of cathode flow channels and CO_2 mole fractions. Fig. 15 shows the distribution of CO_2 mole fraction from B_1 (matrix surface) to B_2 (cathode gas flow channel). As shown in Figs. 14 and 15, there were mole fraction drops across the current collector. Differences of CO_2 mole fraction between B_1 and B_2 for CC1, CC2, and CC3 were 9.72×10^{-3}, 2.97×10^{-3}, and 16.58×10^{-3}, respectively. CC2 showed the smallest difference. Also, the CO_2 mole fraction at B_1 had highest value in CC2.

CO_2 mole fractions of three cases were compared in the x–z plane. Fig. 16 presents the distribution of CO_2 mole fraction from B1 to B2 of three cases. Differences of CO_2 mole fraction between maximum and minimum of CC1, CC2, and CC3 were 2.57×10^{-3}, 0.62×10^{-3}, and 6.78×10^{-3}, respectively. Mole fraction difference of CC2 showed the smallest difference. CC2 which has the largest gas open area to electrodes caused efficient gas distribution characteristics both in the thickness and transverse directions. As well as CO_2 distribution in the cathode side, there were gas mole fraction differences in other gas species.

There are two modes in species transports. Species were transported by the laminar flow of mixture gases in the gas flow channel. Species were transported and supplied to reaction site (B_1) by diffusion in electrodes. Connected regions between electrodes and gas flow channels are the gas open area of electrodes which is formed by the current collector. Differences of the mole fraction among three cases come from the differences of

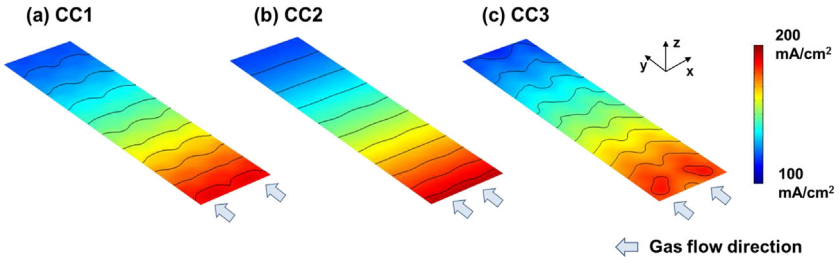

Fig. 12. Current density distributions at 150 mA/cm^2.

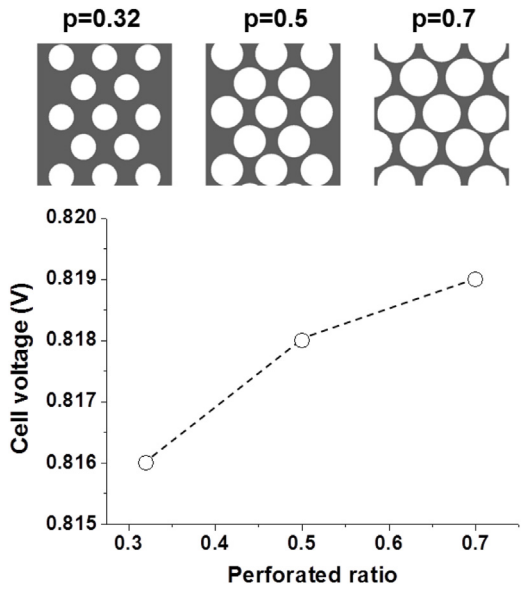

Fig. 13. Distribution of cell voltages at 150 mA/cm^2 according to the perforated ratio.

the gas open area of the current collector. Large perforated ratio increases the gas open area to electrodes and the amount of reactive gases diffused into electrodes. With the large gas open area to electrodes, species are more easily diffused in all directions and the differences of gas mole fractions were reduced.

Therefore, a current collector structure with large gas open area to electrodes reduces differences of gas mole fractions between gas flow channel and electrodes like CC2. It means that reactive gases are supplied efficiently to reaction sights. Consequently, Nernst loss, and cathode polarization loss of CC2 decreased as mentioned in Table 2. The cell voltage of CC2 at 150 mA/cm^2 was the highest among the three cases.

Current collector structures for improved performances

The current collector having a large gas open area to electrodes improves the cell performance. The contact area between the electrodes and the current collector should be minimized to increase the gas open area to electrodes. However, the reduced contact area results in increased stress concentration in electrodes. In such conditions, electrodes cannot be maintained and fracture on the surface occurs. Fracture in the electrodes and matrix induce gas crossover, which is the critical problem of long-term operation [31].

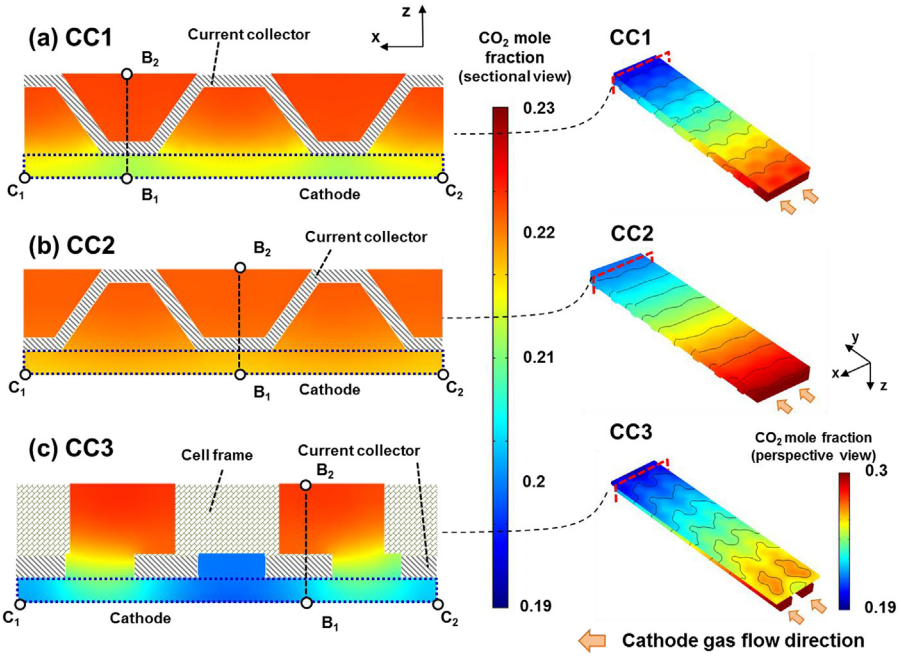

Fig. 14. Cross section of the flow channel and CO_2 mole fractions.

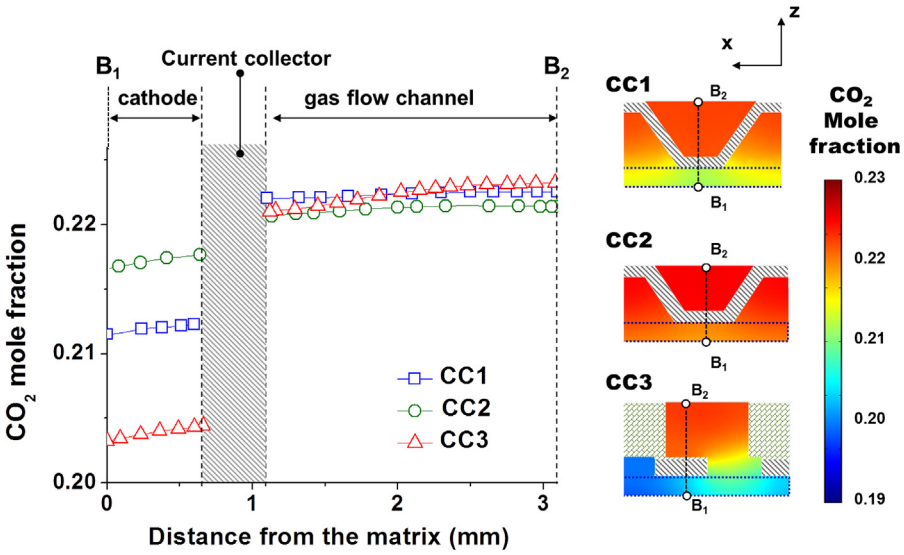

Fig. 15. Distribution of CO_2 mole fraction from the matrix surface (B_1) to the cathode gas flow channel (B_2).

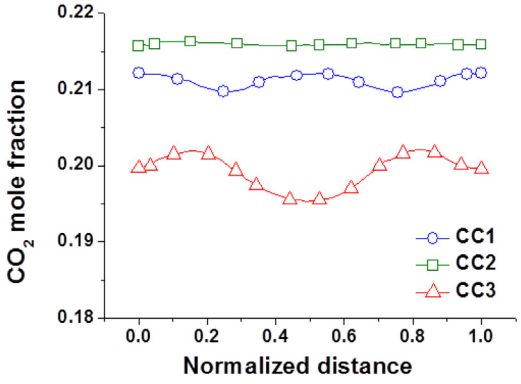

Fig. 16. Distribution of CO_2 mole fraction from B1 to B2.

To increase the performance and long-term operational capabilities, the current collector should have a large gas open area especially for the cathode side, because the cathode side has a larger effect on the performance. At the same time, the current collector should make a stable contact between current collectors and electrodes. For those reasons, strengthened electrodes or electrodes with a mesh structure [32] should be employed.

Conclusion

In this work, effects of the current collector on MCFCs were investigated numerically and experimentally. Three types of current collectors were employed in the experiments and simulation. In simulation results, voltages at 150 mA/cm^2 for CC1, CC2 and CC3 were 0.823 V, 0.832 V, and 0.816 V, respectively. The performance of CC2 which has the largest gas open area shows the best performance. Amount of reactive gases diffused into electrodes increased when the current collector with a large gas open area to electrodes was employed. Difference of gas mole fractions between gas flow channel and electrodes were reduced. As a result, Nernst loss and cathode polarization loss decreased. Current collectors having a large gas open area and ensuring stable contact between components enhance the cell performance and potential for long-term operation.

Acknowledgment

This work was supported by the KIST In-house Program (2E26590), the KETEP Renewable Energy R&D Program (No. 20143010031830 and No. 20163030031860) and GRL research program of KIST.

References

[1] X. Li, Principles of Fuel Cells, Taylor & Francis Group, New York, 2005.
[2] B.H. Choi, H.J. Sung, Int. J. Hydrogen Energy 39 (2014) 12913.
[3] X. Li, I. Sabir, Int. J. Hydrogen Energy 30 (2005) 359.
[4] W.M. Yang, S.K. Chou, C. Shu, J. Power Sour. 164 (2007) 549.
[5] R. Chen, T.S. Zhao, Electrochim. Acta 52 (2007) 4317.
[6] X.H. Yan, T.S. Zhao, L. An, G. Zhao, L. Zeng, Electrochim. Acta 139 (2014) 7.
[7] S. Shimpalee, S. Greenway, J.W. Van Zee, J. Power Sour. 160 (2006) 398.
[8] S. Shimpalee, J.W. Van Zee, Int. J. Hydrogen Energy 32 (2007) 842.
[9] J. Wang, Appl. Energy 157 (2015) 640.
[10] A. Ghanbarian, M.J. Kermani, Energy Conv. Manage. 110 (2016) 356.
[11] H. Hirata, T. Nakagaki, M. Hori, J. Power Sour. 83 (1999) 41.
[12] F. Yoshiba, N. Ono, Y. Izaki, T. Watanabe, T. Abe, J. Power Sour. 71 (1998) 328.
[13] Z. Ma, S.M. Jeter, S.I. Abdel-Khalik, Int. J. Hydrogen Energy 28 (2003) 85.
[14] H. Kim, J. Bae, D. Choi, Int. J. Hydrogen Energy 38 (2013) 4782.
[15] Y.J. Kim, I.G. Chang, T.W. Lee, M.K. Chung, Fuel 89 (2010) 1019.
[16] J.-H. Koh, B.S. Kang, Int. J. Energy Res. 25 (2001) 621.
[17] F. Yoshiba, Int. J. Energy Res. 28 (2004) 1361.
[18] C.-W. Lee, M. Lee, M.-J. Lee, S.-C. Chang, S.-P. Yoon, H.C. Ham, et al., Int. J. Hydrogen Energy 41 (2016) 18747.
[19] W. Vielstich, A. Lamm, H.A. Gasteiger, Handbook of fuel cells: fundamentals technology and applications, Fuel Cell Technology and Applications, vol. 4, Wiley, 2003.
[20] C.-W. Lee, D.-Y. Yang, D.-W. Kang, T.-W. Lee, Int. J. Hydrogen Energy 39 (2014) 6714–6728.
[21] J.-H. Koh, B.S. Kang, H.C. Lim, J. Power Sour. 91 (2000) 161.
[22] C. Yuh, J. Selman, J. Electrochem. Soc. 138 (1991) 3642.
[23] J. Brouwer, F. Jabbari, E.M. Leal, T. Orr, J. Power Sour. 158 (2006) 213.
[24] J.-H. Koh, H.-K. Seo, Y.-S. Yoo, H.C. Lim, Chem. Eng. J. 87 (2002) 367.
[25] V. Verda, A. Sciacovelli, Appl. Therm. Eng. 31 (2011) 2740.
[26] L.J. Blomen, M.N. Mugerwa, Fuel Cell Systems, Springer Science & Business Media, 2013.
[27] M. Baranak, H. Atakül, J. Power Sour. 172 (2007) 831.
[28] COMSOL Multiphysics v4.2, COMSOL Inc., 2014.
[29] D.Y. Goswami, F. Kreith, Handbook of Energy Efficiency and Renewable Energy, Crc Press, 2007.
[30] H.V.P. Nguyen, M.G. Kang, H.C. Ham, S.H. Choi, J. Han, S.W. Nam, et al., J. Electrochem. Soc. 161 (2014) F1458.
[31] C. Yuh, J. Colpetzer, K. Dickson, M. Farooque, G. Xu, J. Mater. Eng. Perform. 15 (2006) 457.
[32] H.V.P. Nguyen, S.A. Song, D.-N. Park, H.C. Ham, J. Han, S.P. Yoon, et al., Int. J. Hydrogen Energy 37 (2012) 16161.